3D-Printable Thermoactive Helical Interface with Decentralized Morphological Stiffness Control for Continuum Manipulators

S.M.Hadi Sadati[1,2,3], Luis Sullivan[2], Ian D. Walker[4], Kaspar Althoefer[5] and Thrishantha Nanayakkara[3]

***Abstract*— We present a 3D-printable thermoactive scale jamming interface as a new way to control a continuum manipulator dexterity by taking inspiration from the helical arrangement of fish scales. A highly articulated helical interface is 3D-printed with thermoactive functionally graded joints using a conventional 3D printing device that utilizes UV curable acrylic plastic and hydroxylated wax as the primary and supporting material. The joint compliance is controlled by regulating wax temperature in phase transition. Empirical feed-forward control relations are identified through comprehensive study of the wax melting profile and actuation scenarios for different shaft designs to achieve desirable repeatability and response time. A decentralized control approach is employed by relating the mathematical terms of the Cosserat beam method to their morphological counterparts in which the manipulator local anisotropic stiffness is controlled based on the local stress and strain information. As a result, a minimalistic central controller is designed in which the joints' thermo-mechanical states are observed using a morphological observer, an external fully monitored replica of the observed system with the same inputs. Preliminary results for passive shape adaptation, geometrical disturbance rejection and task space anisotropic stiffness control are reported by integrating the interface on a continuum manipulator.**

I. INTRODUCTION

Performing complicated tasks such as manipulation in unpredictable conditions, where safe interaction with the environment is important, requires dexterity and compliance in which low actuation energy, high dexterity, reachability, maneuverability, back drivability and self-adjustability of continuum mechanisms have proven to be advantageous. However, compliance has disadvantages such as uncertain deformations, limited control feedback, reduced control bandwidth, stability issues and underdamped modes where high stiffness and damping modes are required to achieve precision in tasks involving working against external loads [1], [2]. As a biological solution, natural skin, especially with scales as flexible armor in animals such as fish, turtles, armadillos and snakes, show stiffness regulation in response to irritation or penetrating forces. The scales slide almost freely in general movements, but are jammed as a result of penetration forces while the overlapping area increases due to inward bending of the skin to provide even more protection [3]. However, the role of passive or active scale jamming on the animal body stiffness regulation has not yet been addressed adequately.

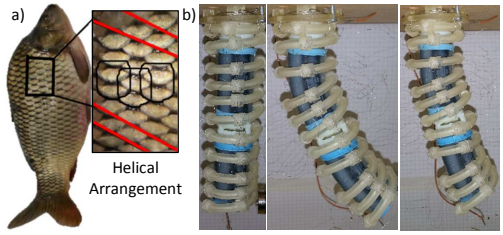

Fig. 1. (a) Overlapping and helical arrangement of scales in a Cyprinus Carpio fish, (b) the thermoactive interface integrated on a two module STIFF-FLOP continuum manipulator for stiffness control (left & middle) and shape locking (left & right) in the straight and bent configurations.

Jamming as a means for stiffness control, by modulating the shear forces due to Coulomb and viscous damping between the jammed and interlocking media, has been utilized in design of variable stiffness manipulators [4], [5], [6] of which a comparative study by Wall shows the advantages of a layer jamming arrangement [7]. tendon-driven jamming is introduced recently to overcome controllability and portability limitations of vacuum enabled jamming in underwater and space applications [8], [9]. The jamming media behaves similarly to a ductile material that undergoes an elastic followed by a plastic deformation in which the elastic deformation threshold (yield) is a function of the friction between the jamming media controlled by the normal force on the contacting surfaces. A high hysteresis is a result of this behavior and the external load should be kept below the yield threshold for an almost linear and repeatable behavior. This behavior is similar to the stiffness change due to phase and glass transition in low melting point (LMP) alloys, such as field's metal [10], [11], and composite material with inherent thermal instability, such as wax [12] and ABS [13]. This class of material is used in much recent research due to higher stiffness range (4.65-5.76 times increase in the stiffness [13]), easy electrical modulation through heating, self-healing properties and 3D printable fabrication compared to other stiffening mechanisms [1], [10]. However, the thermoactive design suffers from slow response time in the cooling process, poor controllability and repeatability due to complex phase transition, low efficiency due to heat dissipation, sensitivity to ambient temperature and safety issues due to high current and temperature which

This work is supported by the U.K. Engineering and Physical Sciences Research Council (EPSRC) Grant: EP/N03211X/2, European Union H2020 project FourByThree code 637095, and Leverhulme Trust Project RPG-2016-345.

[1]S.M.Hadi Sadati is with the Department of Engineering Mathematics, University of Bristol, Bristol, UK. s.m.hadi.sadati@bristol.ac.uk

[2]S.M.Hadi Sadati and Luis Sullivan are with the Department of Informatics, King's College London, London, UK.

[3]S.M.Hadi Sadati and Thrishantha Nanayakkara are with the Dyson School of Design Engineering, Imperial College London, London, UK.

[4]Ian D. Walker is with the Department of Electrical and Computer Engineering, Clemson University, Clemson, USA.

[5]Althoefer Kaspar is with the Department of Mechanical and Material Science, Queen Mary University of London, London, UK.

are not adequately addressed in recent studies [1], [12], [13], [11]. These should be addressed with proper structure and control design and implementation of a cooling mechanism based on the final application. Thermoactive materials are more suitable for applications in cold ambient temperature where rapid cooling improves the system response time and repeatability, e.g. underwater [14], space and high attitudes [15], [16], and for static tasks, e.g shape locking for continuum manipulators [6] and robotic surgeries with mostly quasi-static operations [1], [2], [5], [11]. A recent review of stiffening solutions for continuum manipulators by Blanc, et. al. shows the advantages of shape locking mechanisms to achieve higher stiffness values and low melting point material for higher stiffening ratio [1].

Planning and control of stiffness reconfigurable mechanisms require cumbersome analytical and computation tools for which the idea of exploiting the embodied intelligence or morphological computation of the available physical hardware has been introduced [17], [18]. By breaking a complex control problem into simple sub-problems, a decentralized control system is formed that benefits from parallel execution and lack of communication delay where the tasks are fulfilled based on simple repetitive actions with limited local sensory feedback and computation capabilities [19].

In our previous work, we presented a tendon-driven interlocking scale jamming design inspired by the helical arrangement and morphology of the fish scales (Fig. 1.a) to control torsional stiffness of a helical interface cross-section. As a result, we achieved a simpler design and actuation method which, for the first time, provides better wearability, linear behavior and lower hysteresis as well as high load-bearing capacity and linear stretch in uniform actuation [9] compared to the previous locking and jamming designs [1]. It should be noted that biomimicry is not the objective of this study. Rather, we aim to test the hypothesis that contact friction/locking control using scales is a viable method for stiffness control of exoskeletons for soft robots. However, such design may be useful to uncover or test hypotheses about the operation of biological structures [14], [17], [19]. While usually the jammed surfaces normal force is controlled for stiffening, recently, we investigated the idea of using a novel thermoactive shape memory Velcro mechanism between the layers [20].

To achieve higher load-bearing range, simpler actuation mechanism, smaller setup design and, most importantly, local anisotropic control over the stiffness tensor, in this paper, we investigate how the inter-scale elasticity and damping for the same helical interface can be controlled by phase transition temperature control of an LMP composite wax in a 3D-printable functionally graded thermoactive joint design. As a result, our design benefits from the advantages of an interlocking design and using low melting point material. First, a design overview is presented in section II. A new two-step mathematical model is proposed in section III. The manipulator mechanics is modeled with variable curvature (VC) kinematics via the Cosserat beam method [21] and the stiffness tensor of the rounds of scales in each element

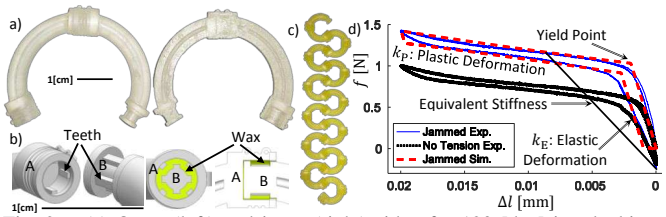

Fig. 2. (a) Outer (left) and inner (right) side of a 120 [deg] interlocking scale with functionally graded thermoactive joints, (b) a thermoactive joint design, (c) a 3D-printed interface before forming into a helix with 135 [deg] scales, (d) deformation regions and definition of equivalent stiffness based on the results for a tendon-driven scale jamming interface in [9].

is found using the Principle of Virtual Work (PVW). Mean values for an element elastic coefficient are found based on the joints' elastic and plastic deformations. A decentralized morphological controller is introduced in section IV to simplify the problem of shape adaptation and stiffness regulation in response to external geometrical disturbances. The novel idea of morphological observer is introduced, where the system states are estimated based on the measurements from an external fully monitored joint with the same design and control signal. The repeatable characteristics of such joints are investigated based on the phase transition profile of the LMP hydroxylated wax and for different joint designs and actuation scenarios, and experimental relations are identified to implement forward control of such joints in section V. In section VI, experiments are carried out to investigate the performance of the modeling and forward control for the interface uniform and anisotropic stiffness regulation while the states are observed with the morphological observer. Finally, the proposed decentralized controller is briefly tested for shape adaptation and task space stiffness regulation in presence of geometrical disturbances. Supplementary video and explanation files about the experiments are provided too.

II. A 3D-Printable Thermoactive Interface

UV curable Thermally stable acrylic plastic (elasticity modulus, $E = 3.2$ [GPa]) and low melting point hydroxylated wax (melting point of 55-65 [°C]) are widely used in high definition 3D printing as the main and the supporting material, where the support material is removed in an oven or hot water after the process. A helical interface with single-axis revolute joints is designed (Fig. 2.a,b) to be printed as a whole unit (Fig. 2.c). A small empty space is left in the joint which is filled with the wax support material in the printing process and small clearances of 0.15 [mm] in diameter and length are considered for free rotation of the joints while preventing the wax from escaping. Four non-contacting teeth with 0.6 [mm] height are designed to increase the joint surfaces engagement with the wax. Based on the von Mises yield criterion, the tooth surface should be larger than 0.58 times the shear surface, so the material withstands the teeth bearing force before the shear sliding begins. A spiral path with 7.9 [mm] groove diameter and two small hinges hold three rounds of heating wire with length $l = 7.45$ [mm] in place (Fig. 2.b). The fully assembled interface is printed as a complete unit with a commercially available high definition 3D printer (PROJET HD 3000 Plus from 3D Systems, www.3dsystems.com) without any further

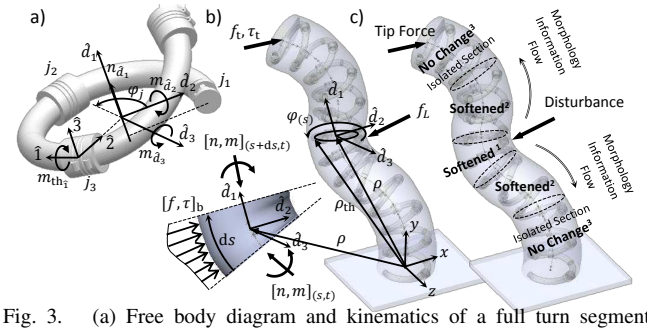

Fig. 3. (a) Free body diagram and kinematics of a full turn segment, (b) VC kinematics and Cosserat rod method parameters for a continuum manipulator, (c) sample information flow in a disentralized stiffness regulation strategy for impedance disturbance isolation in the [1]contacting element, [2]adjacent elements and [3]rest of elements.

modification to the printer. The interface is ready to be used straight away after addition of the heating Nichrome wires (nickel(80%)-chrome(20%) alloy wire, 0.1 [mm] diameter, resistance $R \approx 1[\Omega/\text{cm}]$, from rapidonline.com). The wax is fully jammed when cooled and becomes a lubricant when melted, providing high range of stiffness variability through temperature regulation with small electric actuation. As a result of the small joint design, the small amount of wax forms a thin layer that facilitates heat conductivity and improves stiffness regulation repeatability and response time, while high-performance heating wires are used for efficient temperature control compared to high current (3-5 [A]) Joule heating method in similar research [11]. A 120 [deg] scale curve is suitable for stiffness regulation along the actuation lines of continuum actuators with three pressure chambers, e.g. STIFF-FLOP [2] (Fig. 2.a), a 90 [deg] curve provides decoupled stiffness control in the Cartesian task space (1.b) and a 135 [deg] curve is suitable for a long interface design with smaller number of joints (Fig. 2.c).

III. Modeling Framework

Local stiffness regulation along a continuum manipulator backbone enables simultaneous task space impedance and configuration control as well as disturbance rejection. We assume that each full helix turn adjusts the stiffness coefficient matrices of an element (K_v and K_u) along the manipulator backbone by selective actuation of stiffness controllable joints (Fig. 3.a). The PVW and Castigliano's method are used to find $K_{v|u}$ to be used in the Cosserat rod method describing the manipulator mechanics.

A. Backbone Variable Curvature Mechanics

We use beam theory (Cosserat rod) method as in [22],

$$\begin{aligned} \rho_{,s} &= R(v + [0,1,0]^{\mathrm{T}}),\ R_{,s} = R\,[u]_{\times} \\ v &= {K_v}^{-1}.\left(R^{\mathrm{T}}.(f_{\mathrm{b}} + f_{\mathrm{L}}) + f_{\mathrm{p}}\right) \\ u &= {K_u}^{-1}.\left(R^{\mathrm{T}}.(\tau_{\mathrm{b}} + \tau_{\mathrm{L}}) + \tau_{\mathrm{p}}\right), \end{aligned} \tag{1}$$

where subscript ($_{,x}$) means partial differentiation w.r.t. variable x, $s \in [0, l]$ is the axial position, l is the backbone initial length, $[\hat{d}_2, \hat{d}_1, \hat{d}_3]$ are local curvilinear frame directions, v is the vector of linear strains and u is the vector of curvatures and torsion in the local curvilinear frame, matrix R relates $\epsilon = [v, u]$ to the manipulator Cartesian ($[\hat{i}, \hat{j}, \hat{k}]$) geometry ($\rho$), $[\,]_{\times}$ is an operator to create a skew symmetric matrix, f_{p} and τ_{p} are the actuator loads, $f_{\mathrm{b}} = (l-s)\sigma a_{\mathrm{c}} \mathrm{g}\hat{j}$ is the body weight load, $\tau_{\mathrm{b}} = \sigma a_{\mathrm{c}} \int_s^l \left(\rho_{(s)} - \rho_{(\varepsilon)}\right) \mathrm{d}\varepsilon \times \mathrm{g}\hat{j}$ is the body weight moment, $\tau_{\mathrm{L}} = \left(\rho_{(s_L)} - \rho_{(s)}\right) \times f_{\mathrm{L}}$ is the moment of the external load exerting at $s = s_L$, $a_{\mathrm{c}} = \pi r_{\mathrm{c}}^2$ is the module cross-section area with radius r_{c} and σ is the material density.

B. Helical Interface Kinematics

Assuming no axial twist, for the geometry of a helix (ρ_{h}) with variable curvature backbone we have $\rho_{\mathrm{h}} = R.R_{(2,\varphi)}.[r_{\mathrm{h}}\ 0\ 0]^{\mathrm{T}}$, $\varphi = 2\pi n_{\mathrm{h}} s/l$, where $R_{i,x}$ is a rotation matrix of x around the i^{th} axis, n_{h} is the number of helix turns, l is the backbone initial length and subscript ($_{\mathrm{h}}$) is for the helix parameters [22].

C. Helical Interface Stiffness Model

The load-deformation plot for jamming media usually consists of an elastic followed by a plastic deformation with two distinctive stiffness coefficients (slopes of the $f - \Delta l$ curve in Fig. 2.d), k_{E} for the fully jammed state (elastic region) and k_{P} for when the jammed media begins to slide (plastic region) resulting in stiffness discontinuity, where $f = [n, m]$, n is linear force and m is moment. Here, $k_{\mathrm{E|P}}$ are functions of the material temperature and density. For the first time, we introduce an equivalent stiffness as in Fig. 2.d for continuous stiffness modulation with such design as the ratio of external load to the summation of elastic and plastic deformation. We assume infinite shear, a valid assumption for relatively long continuum manipulators where there is no deformation due to torsion ($m_{\hat{d}_1} \approx 0$) and shear forces ($n_{\hat{d}_2} = n_{\hat{d}_3} \approx 0$) on the manipulator cross-section. Local helix lead angle is assumed to be almost perpendicular ($\gamma \approx \pi/2$) and hence constant [21], [22] and its effects are neglected. Based on the free body diagram (Fig. 3.a), we have $m_{\mathrm{h}} = R^{\mathrm{T}}_{(2,\varphi)}.([r_{\mathrm{h}}\ 0\ 0] \times n + m)$ for the moment in the helix curvilinear frame, where m and n are moment and force, r_{h} is the helix mean radius, φ is the polar angle around $\hat{d}_1$ axis and $\mathrm{C|S}_x = \cos|\sin(x)$. The scale body and the joint act as series elastic elements. Using the PVW, the differential virtual work for the i^{th} scale in each element ($\mathrm{d}w_{\mathrm{sc}_i}$) is

$$\begin{aligned} w_{\mathrm{sc}_i} &= \int_{\varphi_{(i-1)}}^{\varphi_i} \mathrm{d}w_{\mathrm{sc}_i},\ \varphi_i = 2i\pi/n_{\mathrm{sc}}, \\ \mathrm{d}w_{\mathrm{sc}_i} &= (m^2_{\mathrm{h}_{\hat{3}}}/(2EJ_{\hat{3}}) + (m_{\mathrm{h}_{\hat{1}}} + \tau_{\mathrm{y}_i})^2/(2EJ_{\hat{1}}))r_{\mathrm{h}}\mathrm{d}\varphi, \end{aligned} \tag{2}$$

where n_{sc} is the number of scales or joints in a full turn, τ_{y_i} is the yield resistance torque of the i^{th} joint, E is the module of elasticity and $J_{\hat{i}}$ is the scale second moment of area around the $\hat{i}$ principle axis. For the i^{th} joint we have

$$\begin{aligned} w_{\mathrm{j}_i} &= w_{\mathrm{E}_i} + w_{\mathrm{P}_i} + w_{\mu_i},\ w_{\mathrm{E}_i} = \frac{(m_{\mathrm{h}_{\hat{1}}(\varphi_i)} + \tau_{\mathrm{y}_i})^2}{2k_{\mathrm{E}}}, \\ w_{\mathrm{P}_i} &= \frac{(m_{\mathrm{h}_{\hat{1}}(\varphi_i)} - \tau_{\mathrm{y}_i})^2}{2k_{\mathrm{P}}},\ w_{\mu_i} = \frac{\tau_{\mathrm{y}_i}(m_{\mathrm{h}_{\hat{1}}(\varphi_i)} - \tau_{\mathrm{y}_i})}{k_{\mathrm{P}}}, \end{aligned} \tag{3}$$

where w_{E} is the virtual work for the elastic deformation, w_{P} is the virtual work for the plastic deformation and $w_{\mu_{\mathrm{j}}}$ is the virtual energy dissipated by the joint friction. The total energy of each element is $w = \sum_{i=1}^{n_{\mathrm{sc}}}(w_{\mathrm{sc}_i} + w_{\mathrm{j}_i})$.

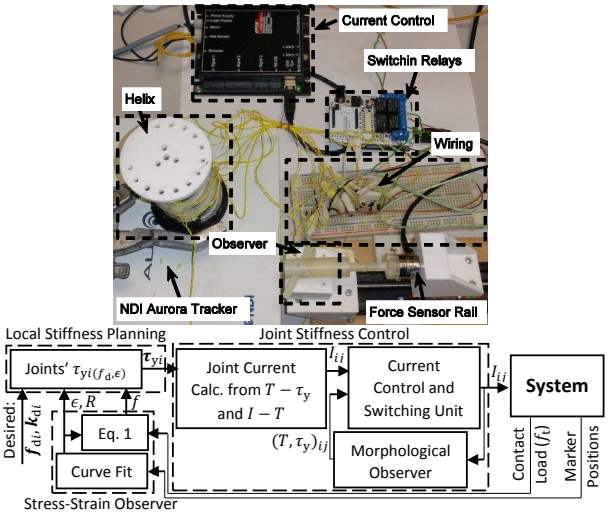

Fig. 4. (top) Experimental control setup, (bottom) a minimal central controller for decentralized impedance regulation. The joint current calculation is replaced with a switching term in the case of simple switching control.

For the equivalent stiffness of the element ($K_{v|u}$), using Castigliano's method, we have $v = w_{,n},\ u = w_{,m}$ and

$$K_v = \text{diag}^{-1}(v).n,\ K_u = \text{diag}^{-1}(u).m, \tag{4}$$

where v, u and K are functions of τ_y and $f = [n, m]$, and for each scale we have the following piecewise rule.

- *Elastic region* ($m_{h_1(\varphi_i)} \leq \tau_{y_i}$ and $\nu_j = 0$): the terms resulting from $w_{P_i,n|m}$ and w_{μ_i} are neglected, and $\tau_{y_i} = 0$ in all other terms.
- *Plastic region* ($m_{h_1(\varphi_i)} > \tau_{y_i}$ or $|\nu_j| > 0$): $[n, m] = 0$ in the terms resulting from $w_{E_i,n|m}$ and $w_{sc_i,n|m}$.

ν_j is relative velocity of the surfaces in plastic deformation. Eq. (4) is rearranged to find $\tau_{y(f,\epsilon)}$ and $\tau_{y(f,K)}$ for stiffness planning and control. The resulting equations for (τ_y) are not independent, since the scales are in series with each other, and the axial and the bending stiffness cannot be controlled simultaneously. Using the symmetry in a formation with four scales in each turn, the element axial stiffness is controlled by $\tau_{y_i} = \tau_{y(f,k_{v_{\hat{f}}})}$ and for the bending stiffness control we have $\tau_{y_1} = \tau_{y_3} = \tau_{y(f,k_{u_{\hat{b}}})}$ and $\tau_{y_2} = \tau_{y_4} = \tau_{y(f,k_{u_{\hat{n}}})}$. Then, we have $K_{v|u} = K_{v|u(f,\tau_y)}$ to be used in Eq. (1).

IV. Morphological Control and Observation

A. Shape Adaptation and Configuration Control

The interface is fully compliant during manipulations featuring passive shape adaptation (Fig. 1.b middle) and can lock any final shape (Fig. 1.b right). A larger reachable configuration space is possible with minimal control inputs and local stiffening of the interface.

B. Decentralized Morphological Control

A model-based decentralized morphological controller is proposed to simplify the complex problem of impedance disturbance rejection at any point along the backbone.

1) Model-Based Control: A simple control law maintains a bias or desired stress by changing local stiffness that can be used for shape adaptation, disturbance isolation and task space impedance control. Local strains (ϵ) are assumed to be known to the local controllers of each element while the stress (σ), distributed along the manipulator, is considered as a morphological signal conveying necessary information between the elements. Any impedance disturbance, e.g. contacting with soft or rigid environment, is canceled through proper shape adaptation. This does not include the case of constant external load. It means that the final disturbed strains (ϵ_e) are known and the goal is to maintain a desired contact force (f_d) for task space impedance control or impedance disturbance isolation by maintaining a bias force distribution similar to before the disturbance $f_0 = K.\epsilon_0$, where ϵ_0 is the initial strain before the disturbance. The stiffness for the element at the contact point is found from $\tau_{y(f_d,\epsilon_e)}$ (Fig. 3.c[1]). The stiffness of the adjacent elements are adjusted to maintain the bias load distribution of the undisturbed structure (f_0) with the disturbed configuration (ϵ_e) using $\tau_{y(f_0,\epsilon_e)}$ (Fig. 3.c[2]). As a result, the local disturbance is isolated and no change in the rest of elements are necessary (Fig. 3.c[3]). The interface is looked in the new configuration.

2) Simple Switching Control: The contacting and adjacent elements are fully softened to reach f_d or f_0 through passive shape adaptation and then are solidified.

C. Minimal Central Controller

1) Central Controller Design: A simple central controller, as in Fig. 4, can be designed based on the proposed decentralized control paradigm, where a switching relay unit connects a single current controller unit to each of the joints one at a time to regulate their temperature and stiffness with a time period less than the system response time. The manipulator geometry (ρ and R) is found by interpolating a polynomial through tracked points along the manipulator, using magnetic tracking sensors [21], based on which the elements' load distribution ($f = [n, m]$) and ϵ are observed using Eq. (1).

2) Joint Morphological Observer: Empirical feedforward relations are used to control the joint yield torque (τ_y) and temperature (T). However, these values cannot be measured directly to implement a feedback controller due to the large number of joints, sensor size and space limitation. The concept of morphological observer is thus introduced, which is a fully monitored replica of the observed system with the same inputs. Similar to a conventional observer where a computer model is used to estimate inaccessible states, here we use a physical model for state estimation. An exactly similar joint with all the necessary sensors is designed (Fig. 5.f) and equivalent currents are supplied to the observed joint and replica. The system yield torque (τ_y) and temperature (T) are estimated and controlled based on the morphological observer readings. The observation accuracy is prone to working condition differences of the replica and system, e.g. orientation and ambient temperature.

V. System Thermo-Mechanical properties

High-performance Nichrome wire is used as a robust low current and efficient heating element. The wire resistance is found to be $R \approx 1[\Omega/\text{cm}]$ with time constant, the time that a thermistor temperature is dropped by 63.2%, equal to 8.1 [s]. A Maxon Motors EPOS2 5/50 is used for current

control of the heating wire. initially, a simple switching (Bang-Bang) controller is used to regulate the system mean temperature. The temperature is measured using a K-type thermocouple and a National Instruments NI-DAQmx 6210 for signal amplification, noise canceling and analog to digital conversion. A HIWIN KKA40 precision linear actuator is used for accurate linear displacement and an ATI-Nano17 6-axis force sensor is used to measure the quasi-static loads.

A. Wax Melting Temperature and Pattern

The melting pattern, surface friction and shear stress of the hydroxylated wax support material are investigated. A cylinder (20 [mm] inner diameter and 20 [mm] height) is filled with the hydroxylated wax while heated with a 0.3 [mm] diameter spiral Nichrome wire at the center passing a 200 [mA] current. The thermocouple tip is placed in the middle (10 [mm] height) and with 4 [mm] radial distance from the inner surface. The support material had a cream color in the solid state. The melting starts around the heating wire while the material color turns to brown. The wax state starts at ≈40 [°C] and stabilizes at ≈45 [°C]. The melting starts at ≈55 [°C] propagating from the vicinity of the heating spiral from top to bottom, due to natural heat convection in the melted wax, and stabilizes in ≈65 [°C] until the whole material is fully melted in about ≈6 minutes. While cooled, the solidification starts at ≈55 [°C], trapping the air bubbles in the material, from the outer surfaces and completed in ≈22 minutes with free air cooling and in ≈11 minutes in water, both at room temperature ($T_0 = 26$ [°C]). Small heat conductivity of the wax results in a slow nonuniform transition pattern with visible borders (Fig. 5.a). While a large transition state is preferable for continuous stiffness control, compared to rapid melting of most LMP alloys [10], [11], a small enclosed volume should be designed to achieve uniform and fast response actuation.

B. Wax Shear Strength, Surface Friction and Stiffness

The same cylinder is covered with a cap and two shaft designs, a smooth cylinder to measure the resisting torque (τ) and shear stress (σ_{shear}) due to surface friction, and a toothed design to calculate the same values for the material yield stress (Fig. 5.b). The effective radius, where the breaking starts, is 5 [mm], similar to the shafts' base radius and $h_{\text{w}} = 12$ [mm] is the shaft active height The heating wire is placed on the joint outer surface where the melting starts. While precise high-resolution temperature regulation of the joint is possible, a step change of 10 [°C] is used in the experiments considering our real application with a smaller joint design. The temperature is not measured at the effective radius and is used only for comparison purpose. The yield and breaking values for the wax rigid state ($T < 40$ [°C]) is not reported due to force sensor saturation and damage to the joint structure. These values are reported for the final smaller joint design. Three full cycles of actuation are carried out in each experimental trial (Fig. 5.e). The material behaved like a brittle material in the first actuation cycle, where the resisting force sharply drops (Fig. 5.c 1st

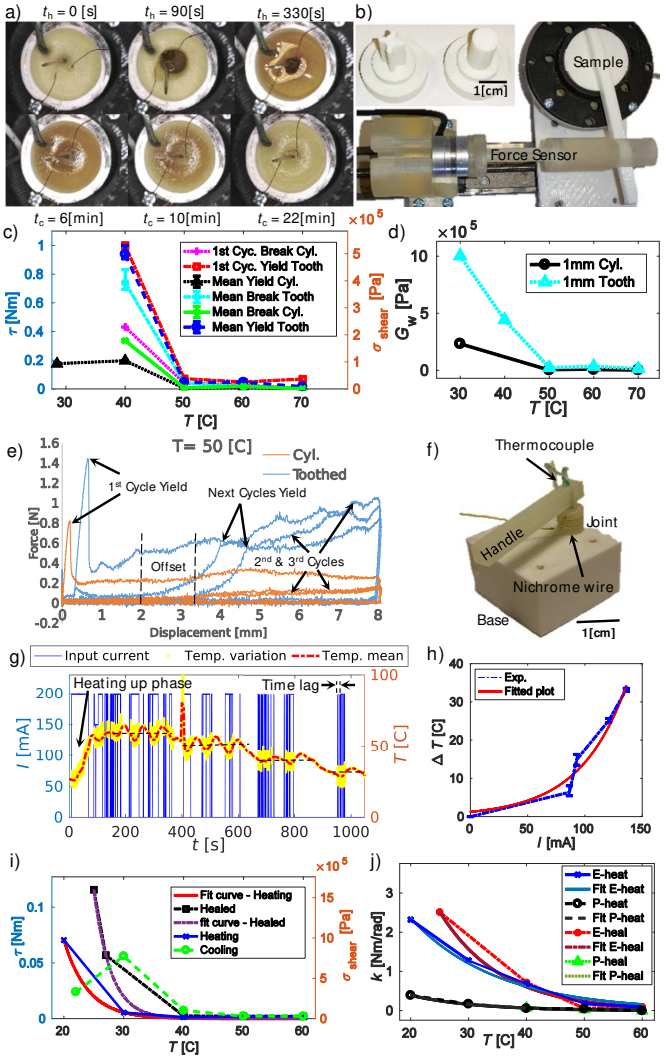

Fig. 5. (a) Wax melting pattern, (b) cylindrical and toothed shaft designs and experiment setup, (c) yield and breaking torque and shear stress vs. temperature, (d)shear modulus vs. temperature for small (1 [mm]≈1.16 [rad]) deformation, (e) sample results of repetitive actuation for both designs at T=50 [°C]. Electro-thermo-mechanical characteristics of a single 3D-printed functionally graded joint in room temperature ($T_0 = 26$ [°C]): (f) a sample joint with temperature sensor at the center which is used as a morphological observer, (g) temperature and current plot for initial switching bang-bang feedback control, (h) mean current vs. mean temperature differences (ΔT), (i) torque and shear stress vs. temperature for heating, cooling and healing control strategies, (j) joint stiffness (k) in elastic (E) and plastic (P) deformations.

Break/Yield and Fig. 5.e), but more like a ductile material for the next cycles with distinctive yield point, where the plastic deformation begins (Fig. 5.c Mean Yield and Fig. 5.e), and breaking point, where the resisting force drops (Fig. 5.c Mean Break). The breaking torque is higher for the first cycle especially for the cylindrical shaft (≈%71) while in the toothed design this value is (≈%9). The mean yield strength of the toothed design is 4.5 times higher than the smooth cylindrical one showing higher shear stress strength compared to the surface viscosity and friction between the joint shaft and the wax. Variation of the material mean yield stress is noticeable, 8-500 [KPa] for the toothed design and 1-180 [KPa] for the cylindrical design, with a relatively sharp drop at the wax transition temperature especially for the cylindrical shaft. To identify the wax shear modulus (G_{w}),

we considered the resisting torque for a small (1 [mm]≈1.16 [rad]) deformation assuming; 1) the wax is fully rigid at the room temperature and the initial measured elasticity is only due to the joint structure (k_{js}), 2) the structure elasticity does not change with temperature. For G_{w} (Fig. 5.d) we have $1/k_{\mathrm{j}} = 1/k_{\mathrm{js}} + h_{\mathrm{w}}/(G_{\mathrm{w}} J_{\hat{t}_{\mathrm{w}}})$, where k_{j} is the joint measured stiffness, $J_{\hat{\mathrm{i}}_{\mathrm{w}}} \approx 3e-7\ [m^4]$ is the wax cross-section second moment of area and $h_{\mathrm{w}} = 12$ [mm] is the wax height.

The joint has a complex behavior with linear elastic stiffness in the first cycle but an increasing value for the later cycles (Fig. 5.e). While the yield strength of the 2nd and 3rd cycles are almost equal, the transition is delayed with an offset, especially in lower temperatures, resulting in a different equivalent stiffness. This is due to the wax melting pattern, self-healing properties and its porous structure variable density. The non-smooth stick-and-slip behavior in the wax state (plastic deformation) results in a large hysteresis in a full actuation cycle and poor repeatability at the wax transition temperature for continuous operations. To achieve better repeatability and response time, we continue with a small toothed design and the characteristics of the first actuation cycle is used for the controller design due to better stiffness range, linear behavior and a smoother stiffness-temperature profile. Besides, a small enclosed wax volume is considered to reduce the variability of the wax properties at the transition temperature (Fig. 5.f).

C. A Single Joint Electro-Thermo-Mechanical Relation

A joint, as explained in section II (Fig. 2.b), is fabricated with a handle and a temperature sensor at the joint center (Fig. 5.f). The measured temperature at the joint center does not represent the wax temperature and the properties of the whole system are identified in this section. A similar test setup as in Fig. 5.b and a switching control are used. Empirical relations for mean values of current-temperature ($I-T$), temperature-yield torque ($T-\tau_{\mathrm{y}}$) and temperature-elastic and plastic stiffness ($T-k_{\mathrm{E|P}}$) are identified to be used for feed-forward control. The mean heat capacity coefficient of the system is found to be 0.45 [J/°C] from the nearly linear initial heating stage of the temperature control experiments (Fig. 5.g). It takes 70 [s] to melt (50 [°C]) and 120-240 [s] to solidify the wax, 6-12 times faster than the bulky setup in section V-B, with ≈14.5 [s] lag between the current actuation and the temperature increase, almost independent of the temperature, due to the material low thermal conductivity. The $(I-T)$ relation (Fig. 5.h) is

$$T = C_{\mathrm{I}} 1.235\ \mathrm{e}^{24.4I} + T_0, \tag{5}$$

where C_{I} is a correction factor, mainly due to the change in the heat dissipation coefficient, to be set before each run and based on a measurement with the morphological observer. The variation in the temperature is significant using a switching controller due to the system large thermal response time and inertia. A 5-6 times higher resistance torque for the first actuation cycle, a small drop ($\approx 20-25\%$) for the next cycles and an offset in the initial position due to the system hysteresis are observed as in the previous section. The breaking point of the first cycle is considered for the control design (Fig. 5.i). Three temperature regulation strategies are tested; 1) heating, where the desired temperature is higher than the current temperature, 2) cooling, where the desired temperature is lower, 3) healing, where the wax is fully melted at 50 [°C] then cooled (healed) to the desired temperature. τ_{y} varies based on the initial T for the heating and cooling strategies where continuous control is possible. The cracks, remained from previous tests, results in an undesirable drop in τ_{y} in the cooling strategy (Fig. 5.i). The healing process provides higher τ_{y} and smoother $T-\tau_{\mathrm{y}}$ relation if executed either very quickly or when the interface is not loaded. We continue with heating strategy for continuous actuation and healing strategy for static or reducing temperature scenarios. τ_{y} is identified as

$$\tau_{\mathrm{y_{heat}}} = 10.69\mathrm{e}^{-0.251T},\ \tau_{\mathrm{y_{heal}}} = 764.1\mathrm{e}^{-0.3518T}. \tag{6}$$

The small joint design results in an almost constant and repeatable stiffness during the tests and a smooth variation w.r.t. T. $k_{\mathrm{E|P}}$ for the joint are identified as (Fig. 5.j)

$$\begin{aligned} k_{\mathrm{E_{heat}}} &= 9.017\mathrm{e}^{-0.06715T}, k_{\mathrm{P_{heat}}} = 2.328\mathrm{e}^{-0.08929T} \\ k_{\mathrm{E_{heal}}} &= 27.37\mathrm{e}^{-0.09533T}, k_{\mathrm{P_{heal}}} = 12.83\mathrm{e}^{-0.1295T}. \end{aligned} \tag{7}$$

Eq. (5-7) are used for feed-forward control, to minimize the temperature variation seen in Fig. 5.g,h, while a switching controller is used to compensate any feedback error.

VI. Interface Experiments and Integration

A. Model-Based Observation and Control

The model-based observation and control method is used for uniform axial and bending stiffness control of a helical interface sample with 3.5 active turns and 120 [deg] scales ($J_3 = 6.3e-11, J_1 = 2J_3$) from an initially straight position (Fig. 6.a,b). The control setup in Fig. 4 is used where the current control unit is connected to the common input of an Arduino relay shield controlled by an Arduino Uno SMD Rev3 board. Each relay is connected to a morphological observer and a row of joints, in the same ambient. A HIWIN precision actuator and an ACTUONIX L12 linear actuator (www.robotshop.com) with 10 [mm] stroke are used for axial and bending tests respectively. Three measurements, each with three deformation cycles are carried on for each experiment. All the joints are activated with the same current in the axial test. The bending case has inactive locked joints at the 0 [deg], 40 °C temperature regulated joints ($I = 80$ [mA]) at 120 [deg] and fully melted ones ($I = 200$ [mA]) at 240 [deg] location. The model-based control error are 7.5% (27.5 [N/m]) for axial ($C_1 = 1,\ T_0 = 22°\mathrm{C}$, Fig. 6.a) and 14% (4.3 [N/m]) for bending ($C_1 = 2.1,\ T_0 = 22°\mathrm{C}$, Fig. 6.b) stiffness control at the tip. The axial stiffness range is much higher (0-556 [N/m] in axial, 0-62 [N/m] for 90 [deg] scales and 0-32 [N/m] for 120 [deg] scales in bending) due to lower bending stiffness of a helix; however, the bending test shows better hysteresis and repeatability due to the joins small elastic rotation. Despite easier stiffness control for continuum manipulators with three actuators, the coupled

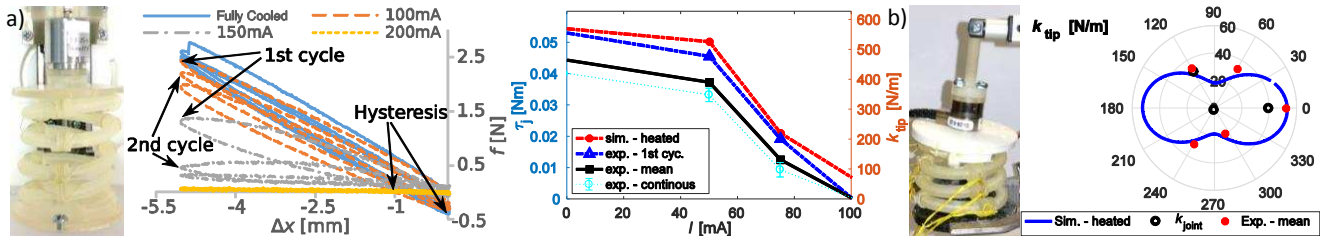

Fig. 6. (a) Model-based control: axial stiffness control, load cycles and achieved stiffness for a helix with 3.5 turns and 120 [deg] scales; (b) anisotropic stiffness control: bending experiment setup and task space stiffness results in polar coordinates.

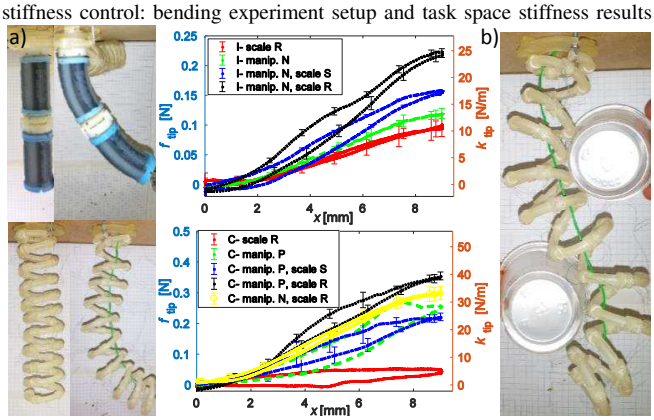

Fig. 7. (a) Results for a two-module STIFF-FLOP continuum manipulator (manip.) and a nine-turn helical interface with 90 [deg] scales (scale) for a 9 [mm] tip lateral deflection in straight (I) and bent (C) configuration (N: inactive, P: pressurized, R: rigid, S: soft), (b) passive shape adaptation.

directional stiffness of 120 [deg] scales results in a smaller maximum stiffness compared to a 90 [deg] one. Our new design has higher stiffness (axial: 22 [N/m], bending: 33 [N/m]) compared to our previous tendon-driven design in similar tests [9]. Despite different orientation of the joints, the observed values were accurate enough to perform the simple stiffness control task in this section.

B. Integration on a Continuum Manipulator

A helical interface with nine turns and 90 [deg] scales is integrated on a continuum manipulator with two STIFF-FLOP (STIFFness controllable Flexible and Learn-able manipulator for surgical OPerations) pneumatic actuator modules [2] for stiffness regulation and shape locking in straight and bent configuration (Fig. 1.b & 7.a). Results for tip resisting force and stiffness of the interface and the module in sole and combined actuation scenarios, with 9 [mm] lateral deflection and $I = 135$ [mA], are presented in Fig. 7.a. The module with complaint scales needs 1.2 [bar] pressure to reach the same configuration as the case with no scale interface and 0.8 [bar]. Large stiffness of the STIFF-FLOP modules, to meet the precision and load-bearing criteria of a robotic surgery, makes the exact shape locking challenging (Fig. 1.b right). Two measurements, each with three deformation cycles are carried out, for each case. Good repeatability is observed due to the manipulator long length resulting in the joints' elastic deformation. The tip stiffness in straight configuration (I) is 12 [N/m] for the rigid (R) scale interface, 13.5 [N/m] for the inactive (N) manipulator, 17.5 [N/m] for the manipulator with soft (S) interface (30% increase due to the added friction) and 25 [N/m] for manipulator with rigid scales (43% increase due to shape locking). These values in bent configuration (C) is 5 [N/m] for the rigid interface (interface shape locking), 29 [N/m] for the pressurized (P) manipulator, 25 [N/m] for the manipulator with compliant interface (14% decrease due to the added weight), 40 [N/m] for manipulator with locked scales (60% increase due to shape locking) and 33 [N/m] for shape locking of the inactive manipulator (Fig. 7.a). The interface resisting force is lower in bending due to a high-value body weight moment at the root joints. The hysteresis due to friction between the manipulator and compliant interface in the straight case, reduces for the bent case where the helical interface acts as a secondary external braid. The total stiffness in the straight case is a summation of the scale and manipulator stiffness; however, this value is higher than a simple summation for the bent case, due to a uniform deformation caused by the manipulator along the interface joints. A lower hysteresis and higher stiffness than expected show the interactive functionality of the interface and pressurized manipulator.

While such design is more suitable for cold environments, e.g. underwater [14], the results are compared with stiffening solutions for medical applications which are extensively studied recently. The tip bending stiffness when integrated on two STIFF-FLOP modules (straight: 2.3-3.3 [N/rad], 47-67 $[\mathrm{KNmm}^2]$, 43% increase, bent: 3.6-5.7 [N/rad], 73-118 $[\mathrm{KNmm}^2]$, 60% increase) is higher than the commercially available endoscopes (15-31 $[\mathrm{KNmm}^2]$) [1], less than the desired value for MIS (17.2 [N/rad]) [5], and similar to low stiffness range granular and layer jamming designs [1]. This design has the best shape locking ability and the highest tip stiffness increase (straight: 43%, bent: 60%) compared to a STIFF-FLOP module with granular jamming (straight: 43%, bent: 18%) [2] and tendon antagonistic stiffening (straight: 94%, bent: 24.3% increase) [23], both with limited shape locking. Local and directional stiffness controllability, higher uniform load-bearing for long designs and similar simple integration are the advantages of the current design compared to our previous tendon scale jamming approach [9]. Besides better scalability, due to omitting tendon routing friction, and local and directional stiffness controllability, the presented design benefits from high load-bearing to weight ratio, axial stretch and simple integration similar to our previous tendon-driven interface [9], but presents lower stiffness increase (straight: 83%, bent: 330%), due to the contribution of the tendon stiffness, and suffers from higher hysteresis, nonlinear behavior and lower repeatability. We plan to address these issues by an improved design based on a detailed heat transfer analysis, passing the interface through a helical tube filled with a coolant fluid, proper isolation of the heating

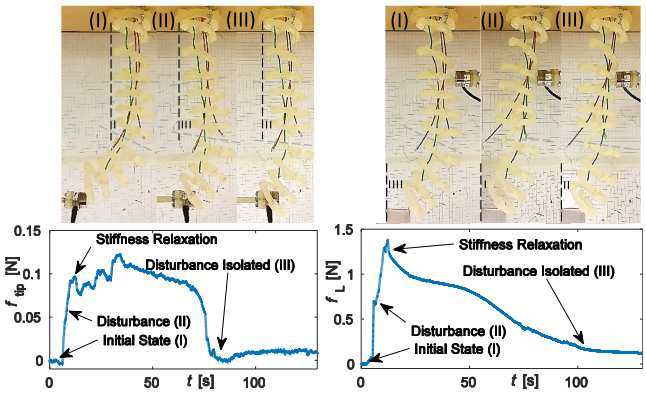

Fig. 8. (left) Preliminary results for tip and (right) backbone disturbance rejection through passive shape adaptation with three independent stiffness controllable elements: initial state (I), disturbance (II), effect isolation (III).

wires, using multiple parallel helical strands and changing the scale dimensions for better shape locking and stiffening.

C. Simple Switching Control

The proposed simple switching controller is successfully used for passive shape adaptation (Fig. 7.b), tip force regulation and isolation (Fig. 8 left), and backbone impedance disturbance isolation (Fig. 8 right) of the helical interface. The stiffness of the three elements along the interface is controlled separately. The simple control method increases the adjacent elements compliance to cancel the external load and isolate its effects through passive shape adaptation. 50% of the configuration at the element borders and 92% of the external force in the tip disturbance case and 33% of the configuration and 91% of the external force in the backbone disturbance case are canceled in less than 90 [s]; however, the recovery is limited due to the system passive adaptation.

VII. Conclusion

A thermoactive scale jamming interface is 3D-printed with a commercially available device as both a new way to control a continuum manipulator dexterity and a method to fabricate general mechanisms with thermoactive functionally graded designs. The interface compliance is regulated by controlling the joints' wax temperature for which empirical relations are identified. The common problems of poor repeatability and response time with low melting point material are addressed with a small wax enclosure design and using empirical relations in the controller design. Novel morphological observation and decentralized control approaches are employed based on which a minimal central controller is implemented. Preliminary results for passive shape adaptation, geometrical disturbance rejection and task space anisotropic stiffness regulation are presented by integration of the interface on a continuum manipulator. Our results show potential of our platform and method for stiffness planing of continuum manipulators, especially for quasi-static operations in cold environments such as underwater and space.

References

[1] L. Blanc, A. Delchambre, and P. Lambert, "Flexible Medical Devices: Review of Controllable Stiffness Solutions," *Actuators*, vol. 6, p. 23, 2017.

[2] M. Cianchetti, T. Ranzani, G. Gerboni, et. al., "STIFF-FLOP surgical manipulator: Mechanical design and experimental characterization of the single module," in *IEEE International Conference on Intelligent Robots and Systems (IROS)*, (Tokyo, Japan), pp. 3576–3581, 2013.

[3] K. Oliver, A. Seddon, and R. S. Trask, "Morphing in nature and beyond: a review of natural and synthetic shape-changing materials and mechanisms," *J. Material. Sci.*, vol. 51, pp. 10663–10689, 2016.

[4] A. Jiang, G. Xynogalas, P. Dasgupta, et. al., "Design of a variable stiffness flexible manipulator with composite granular jamming and membrane coupling," in *2012 IEEE/RSJ International Conference on Intelligent Robots and Systems*, (Vilamoura-Algarve, Portugal), pp. 2922–2927, 2012.

[5] Y.-J. J. Kim, S. Cheng, S. Kim, and K. Iagnemma, "A novel layer jamming mechanism with tunable stiffness capability for minimally invasive surgery," *IEEE Trans. Robot.*, vol. 29, pp. 1031–1042, 2013.

[6] S. Zuo, K. Iijima, T. Tokumiya, and K. Masamune, "Variable stiffness outer sheath with Dragon skin structure and negative pneumatic shape-locking mechanism," *Int J CARS*, vol. 9, pp. 857–865, 2014.

[7] V. Wall, R. Deimel, and O. Brock, "Selective Stiffening of Soft Actuators Based on Jamming," *2015 IEEE International Conference on Robotics and Automation (ICRA)*, pp. 252–257, 2015.

[8] J. L. C. Santiago, I. S. Godage, P. Gonthina, and I. D. Walker, "Soft Robots and Kangaroo Tails: Modulating Compliance in Continuum Structures Through Mechanical Layer Jamming," *Soft Robotics*, p. 21, 2016.

[9] S. M. H. Sadati, Y. Noh, S. E. Naghibi, et. al., "Stiffness Control of Soft Robotic Manipulator for Minimally Invasive Surgery (MIS) Using Scale Jamming," in *Intelligent Robotics and Applications*, Lec. Notes Comput. Sci., pp. 141–151, Springer, Cham, 2015.

[10] I. M. Van Meerbeek, B. C. Mac Murray, J. W. Kim, et. al., "Morphing Metal and Elastomer Bicontinuous Foams for Reversible Stiffness, Shape Memory, and Self-Healing Soft Machines," *Adv. Mater.*, vol. 28, pp. 2801–2806, 2016.

[11] F. Alambeigi, R. Seifabadi, and M. Armand, "A continuum manipulator with phase changing alloy," in *IEEE International Conference on Robotics and Automation*, (Stockholm, Sweden), pp. 758–764, 2016.

[12] N. G. Cheng, A. Gopinath, L. Wang, et. al., "Thermally Tunable, Self-Healing Composites for Soft Robotic Applications," *Macromol. Mater. Eng.*, vol. 299, pp. 1279–1284, 2014.

[13] Y. Yang, Y. H. Chen, Y. Wei, and Y. Li, "Novel Design and 3d Printing of Variable Stiffness Robotic Grippers," *J. Mechanisms and Robotics*, vol. 8, no. c, 2016.

[14] J. Jalbert, S. Kashin, and J. Ayers, "Design considerations and experiments of a biologically based undulatory lamprey AUV," *International Symposium on Unmanned Untethered Submersible Technology (UUST)*, 1995.

[15] C. Cohen, B. Hiott, A. D. Kapadia, and I. D. Walker, "Robot tongues in space: continuum surfaces for robotic grasping and manipulation," vol. 9836, *Int. Soc. Optics Photonics*, 2016.

[16] M. B. Wooten and I. D. Walker, "A Novel Vine-Like Robot for In-Orbit Inspection," *45th International Conference on Environmental Systems (ICES)*, pp. 1–11, 2015.

[17] R. Pfeifer and J. Bongard, *How the Body Shapes the Way We Think: A New View of Intelligence*. MIT Press, 2006.

[18] H. Hauser, A. J. Ijspeert, R. M. Fchslin, et. al., "Towards a theoretical foundation for morphological computation with compliant bodies," *Biol Cybern*, vol. 105, pp. 355–370, 2011.

[19] T. Umedachi, V. Vikas, and B. A. Trimmer, "Softworms : the design and control of non-pneumatic, 3d-printed, deformable robots," *Bioinspir. Biomim.*, vol. 11, no. 2, p. 025001, 2016.

[20] H. Afrisal, S. Sadati, and T. Nanayakkara, "A Bio-Inspired Electro-Active Velcro Mechanism Using Shape Memory Alloy for Wearable and Stiffness Controllable Layers," in *Information and Automation for Sustainability (ICIAfS), 9th Int. Conf. on*, pp. 1–6, 2016.

[21] S. M. H. Sadati, S. E. Naghibi, I. D. Walker, et. al., "Control Space Reduction and Real-Time Accurate Modeling of Continuum Manipulators Using Ritz and Ritz–Galerkin Methods," *IEEE Robot. Autom. Lett.*, vol. 3, pp. 328–335, 2018.

[22] S. Sadati, S. E. Naghibi, A. Shiva, et. al., "A Geometry Deformation Model for Braided Continuum Manipulators," *Frontiers Robot. AI*, vol. 4, p. 22, 2017.

[23] A. Shiva, A. Stilli, Y. Noh, et. al., "Tendon-Based Stiffening for a Pneumatically Actuated Soft Manipulator," *IEEE Robot. Autom. Lett.*, vol. 1, no. 2, pp. 632–637, 2016.